

# Comparison of Prediction Modeling Methodologies for Aeroacoustic Characterization of Hovering sUAS Rotors

Christopher S. Thurman\*, D. Douglas Boyd Jr.†, Benjamin M. Simmons‡  
*NASA Langley Research Center, Hampton, VA, 23681*

This work compares artificial neural network and multivariate orthogonal function modeling methodologies for the prediction and characterization of isolated hovering sUAS rotor aerodynamics and aeroacoustics. Design of Experiments was used to create input feature spaces over 9 input features: the number of rotor blades, rotor size, rotor speed, the amount of blade twist, blade taper ratio, tip chord length, collective pitch, airfoil camber, and airfoil thickness. CAMRAD II and AARON were executed at the points defined by the input feature space to predict aerodynamic and aeroacoustic quantities. These predicted aerodynamic and aeroacoustic data were then used to generate artificial neural networks and polynomial response surface models. The two prediction model methodologies were evaluated over test data previously unseen by the models, which showed good prediction capabilities for both model types, with slightly lower prediction error for the artificial neural networks. A characterization study was performed, which showed that input features correspondent to the spanwise sectional blade lift and drag were the most significant factors to the aerodynamic thrust and power, respectively. It was also shown that the aeroacoustic quantities were highly dependent on variations in rotor speed and size, which affect the Doppler factor for tonal noise and the spanwise Reynolds number for broadband noise.

## I. Nomenclature

$C^N$	=	input feature space with $N$ samples
$c(r)$	=	rotor blade chord distribution, in
$c_{tip}$	=	tip chord length, in
$C_T$	=	thrust coefficient
$f(x_k)$	=	prediction model output
$g(\mathbf{x})$	=	continuous system representation
$M$	=	airfoil camber, %chord
$M_\infty$	=	freestream Mach number
$N_b$	=	number of rotor blades
$OASPL_{BB}$	=	overall sound pressure level integrated over the broadband self-noise, dB
$P_{pred}$	=	power predicted using low-fidelity methods, HP
$Q_{pred}$	=	torque predicted using low-fidelity methods, ft-lb
$R$	=	rotor radius, in
$R_d^2$	=	coefficient of determination
$Re$	=	Reynolds number
$r$	=	rotor blade span location normalized by rotor radius
$SPL_{lo}$	=	loading noise component of the tonal noise at the fundamental blade passage frequency, dB
$SPL_{th}$	=	thickness noise component of the tonal noise at the fundamental blade passage frequency, dB
$T_{pred}$	=	thrust predicted using low-fidelity methods, lb
$TR$	=	taper ratio, $\frac{c_{tip}}{c_{root}}$
$t/c$	=	airfoil thickness, %chord
$x_i^k, \mathbf{x}_k$	=	samples in input feature space pertaining to the $k^{\text{th}}$ input feature

\*Research Aerospace Engineer, Aeroacoustics Branch, MS 461, AIAA Member; christopher.thurman@nasa.gov

†Senior Research Aerospace Engineer, Aeroacoustics Branch, MS 461, AIAA Senior Member; d.d.boyd@nasa.gov

‡Research Aerospace Engineer, Flight Dynamics Branch, MS 308, AIAA Member; benjamin.m.simmons@nasa.gov

$\mathbf{y}_j$	=	$j^{\text{th}}$ output from physical system
$\hat{\mathbf{y}}_j$	=	$j^{\text{th}}$ predicted value of $\mathbf{y}_j$
$\alpha$	=	angle of attack, deg
$\Theta_{obs}$	=	acoustic observer angle relative to rotor plane, deg
$\theta(r)$	=	rotor twist distribution, deg
$\theta_{tw}$	=	linear twist, deg
$\theta_0$	=	collective pitch, deg
$\nu$	=	kinematic fluid viscosity, in <sup>2</sup> /s
$\Omega$	=	rotor speed, RPM

## II. Introduction

THE past decade has seen considerable interest in advanced air mobility (AAM) vehicles, capable of transporting personnel and packages across various environments in a safe and sustainable way. These vehicles are typically comprised of multirotor systems and generally range in size from small unmanned aerial systems (sUAS) to single- or multipassenger vehicles designed for operation in urban environments. Though the AAM industry is growing at a rapid pace, noise is still a large inhibitor toward the development and real-world application of these AAM vehicles, which has motivated research in identifying and characterizing noise sources produced by vehicles such as quadcopters, among other types of sUAS vehicles. The study of these smaller sUAS vehicles, or isolated sUAS vehicle components such as rotors, can not only aid in the design of low-noise AAM vehicles, but also in mission planning and trajectory optimization.

In general, the noise generated by rotors can be separated into two main categories: tonal and broadband. Tonal noise is deterministic in nature, having a periodic dependence on rotor speed, or more specifically, the blade passage frequency (BPF). This type of noise is comprised of two constituents: thickness noise and loading noise. Thickness noise can be defined as noise due to fluid displacement by the rotor blade (i.e., geometry dependent), and loading noise is noise caused by the force exerted on the fluid by the rotor blade surface (i.e., force dependent). Broadband noise, on the other hand, is stochastic (i.e., nondeterministic) in nature.

Many tools exist for predicting both tonal and broadband noise [1–4]. For modeling tonal noise, a wide range of tools with varying fidelity exist: panel methods, blade element momentum theory (BEMT), comprehensive analysis codes (e.g., CAMRAD II, CHARM, and RCAS), traditional Navier-Stokes solvers (e.g., OVERFLOW2, FUN3D, and CART3D), and scale-resolving flow simulations (e.g., direct numerical simulation (DNS), large eddy simulation (LES), and the lattice-Boltzmann method (LBM)). Each of these tools is used to predict unsteady aerodynamic forces, and the resulting acoustic pressures are propagated to arbitrary observer locations using an implementation of the Ffowcs Williams and Hawkins (FW-H) [5] equation. Similar approaches have been used to predict broadband noise directly from unsteady aerodynamic forces using the scale-resolving lattice-Boltzmann method, though at great computational cost [1, 2, 6, 7].

There are three types of broadband noise: blade self-noise, turbulence ingestion noise (TIN), and blade-wake interaction (BWI) noise. Blade self-noise is produced by near wake turbulence scattering over a rotor blade trailing edge (i.e., boundary layer dependent), TIN is caused by the ingestion of inflow turbulence into the rotor system, and BWI noise can be loosely defined as noise caused by blade interactions with rotor wake turbulence. Low-fidelity methodologies for predicting broadband trailing edge noise have been established, such as the theoretical trailing-edge noise model devised by Amiet [8] and the semiempirical self-noise prediction methodology devised by Brooks, Pope, and Marcolini (BPM method) in Ref. [9]. These low-fidelity broadband noise tools are frequently used in practice [1, 3, 10–13]; however, they fail to capture more complex aerodynamically induced noise generation associated with rotorcraft (e.g., TIN and BWI noise [14]). Although these low-fidelity tools only account for broadband self-noise, this type of noise is a dominant broadband noise source, and its inclusion in the overall calculation of AAM vehicle acoustics is fundamentally necessary.

Low-fidelity aerodynamic and aeroacoustic models are often used in the vehicle design stage based on their quick prediction time when compared to higher-fidelity methods; however, their implementation is often arduous due to various tuning parameters and associated input changes based on different operating conditions. These drawbacks may be prohibitive to acoustic optimization-based problems. Because of these drawbacks, prediction modeling approaches have been investigated to model both the aerodynamics and aeroacoustics associated with AAM vehicles and components subject to various geometric and operational conditions [13, 15–18]. These prediction models are capable of modeling highly nonlinear input feature spaces (i.e., regions of experimentation) with minimal user input and take only seconds

for prediction, making them desirable for optimization-based design problems as well as for real-time flight simulation applications.

The purpose of the present research is to develop aerodynamic and aeroacoustic prediction models using two different methodologies, artificial neural network (ANN) modeling and multivariate orthogonal function (MOF) modeling, for both a comparative study and for the characterization of hovering sUAS rotors. Previous work conducted in Ref. [13] used a similar input feature space and training data as in this work with three major disadvantages:

- 1) the twist distribution,  $\theta(r)$ , had a functional dependence on a target thrust value,  $C_{T_{\text{design}}} = f(\Omega, R)$ ,
- 2) the observer location was dimensionally fixed in space,
- 3) and no sensitivity analyses were conducted. Only qualitative comparisons between input factors were provided.

The research entailed in this work addresses these shortcomings and also uses a higher-fidelity aerodynamic prediction tool than that used in Ref. [13], which provides better quality training data and a well-posed prediction modeling experiment to compare different modeling techniques.

### III. Technical Approach

A four-step approach shown in Fig. 1 was employed for both modeling procedures in this work. The first step for both modeling procedures entailed the use of Design of Experiments (DoE) to create input feature spaces consisting of discrete combinations of input feature values. The input feature spaces consisted of various airfoil and rotor geometric parameters as well as operating conditions, which encapsulated much of the sUAS region of operability in hover. Preexisting low-fidelity tools were then used to predict various aerodynamic and aeroacoustic quantities at the design points prescribed within the feature space. Once these data were generated, two prediction modeling techniques, ANN modeling and MOF modeling, were used to develop models to accurately and quickly predict various aerodynamic and aeroacoustic quantities of particular interest to rotorcraft. These prediction models were then used in a comparative study to assess model performance and discern any discrepancies between the two modeling procedures. Lastly, these prediction models were used in a characterization effort to study the effects of each input feature on both the aerodynamics and aeroacoustic tonal and broadband noise.

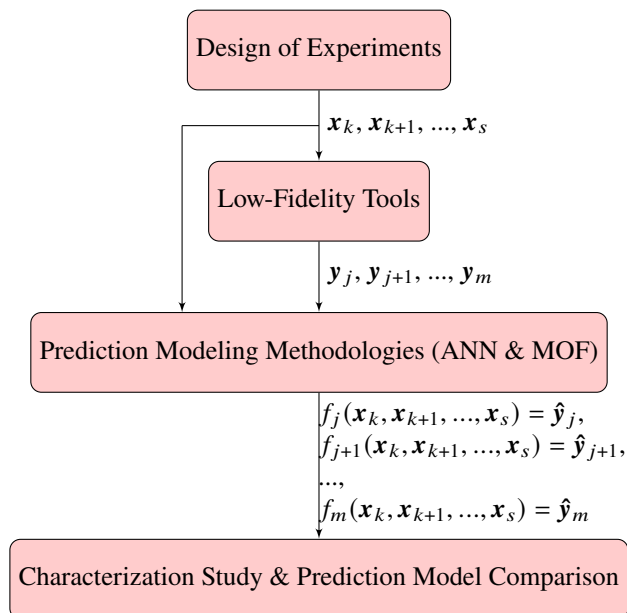


Fig. 1 Block diagram representation of technical approach.

## A. Design of Experiments

DoE is a process used for planning an experiment so that appropriate data can be collected and analyzed by statistical methods, resulting in valid and objective conclusions [19]. This process is typically used in systems comprised of multiple inputs when a nonlinear functional relationship between the responses, such as force and moment coefficients, and the input features is required.

Computer-based experiments, such as those performed in this work, are deterministic in nature. This means that they are only susceptible to systemic error associated with deficiencies related to modeling a physical problem. Typical systemic error arises from grid discretization error, round off error, numerical convergence error, etc., meaning that for a fixed number of iterations, a replicated simulation should produce the same result (i.e., absent of random error). Due to this lack of inherent stochasticism, there is no statistical basis for procedures commonly associated with classical DoE (i.e., factorial designs), such as the analysis of variance (ANOVA). Because of this lack of random error, a space-filling Uniform Design (UD) was used for this work. In general, space-filling designs aim to minimize the difference of the overall mean between the true underlying system,  $g(\mathbf{x})$ , and a prediction model,  $f(\mathbf{x}_k)$ , throughout the design space [20]:

$$\min \left( \left| \int_{C^N} g(\mathbf{x}) d\mathbf{x} - \frac{1}{N} \sum_{i=1}^N f(x_i^k) \right| \right), \quad (1)$$

where  $i$  is the number of samples over the  $C^N$  input feature space.

The deterministic nature of the computer-based experiment in this work makes the prediction modeling effort an interpolation problem, meaning it is imperative to spread the samples in the design space in a manner that best represents the entirety of the experimental domain. The UD has been shown to successfully achieve this goal in previous studies [13, 14] and was selected as the design space for this work. The creation of the UD used in this work followed a threshold-accepting heuristic given by Fang et al. [21], which utilized the modified  $L_2$  discrepancy metric [21, 22], ( $ML_2$ ) as the uniformity criterion. The  $ML_2$  discrepancy was selected in lieu of the commonly used centered  $L_2$  discrepancy due to its superior capabilities in considering the uniformity of samples projected onto all subdimensions of the design space [21]. This method for UD generation was executed using the second generation Aircraft NOise Prediction Program (ANOPP2) DoE Tool (ADOET). ADOET allows for the use of one categorical (i.e., discrete) input feature, such as the number of rotor blades,  $N_b$ . A separate input feature space is designed at each discrete value of the categorical input feature, with their ensemble yielding the final outputted input feature space.

Since  $N_b$  is a categorical input feature, four designs were created, one at each discrete value of  $N_b$ , for a total of 150 design points. The ensemble of these designs was used as the prediction model training data. It is common to split a dataset into training and test data; however, when using DoE, this data split may produce bias toward specific regions of the design space. For example, if all split training data are located in a particular region of the design space, there will be inadequate coverage over the entirety of the design space to train the prediction model. For this reason, ADOET was used to generate a UD for training data and a separate UD consisting of 50 points for test data. Test data are necessary in ML modeling procedures to validate the prediction models against data that were not used in the training procedure. This validation process is vital to ensuring the prediction model can produce accurate predictions everywhere in the design space and can generalize to new data points within the design space, which have not previously been seen by the model during the training process.

The DoE feature space consisted of the following inputs for all prediction models: number of rotor blades,  $N_b$ ; rotor radius,  $R$ ; rotor speed,  $\Omega$ ; linear twist,  $\theta_{tw}$ ; taper ratio,  $TR = \frac{c_{root}}{c_{tip}}$ ; tip chord length,  $c_{tip}$ ; collective pitch,  $\theta_0$ ; airfoil camber,  $M$ ; and airfoil thickness,  $t/c$ . The location of maximum camber was determined to be an insignificant input in Ref. [13] and was held constant at 40% chord throughout this work. The range and type of each input feature are shown in Table 1. Illustrations of the training and test input feature spaces are provided in Fig. 2 where all data points are projected on a 2-D subdimension of the input feature spaces.

**Table 1 Input feature space. (\* indicates categorical factors. All other factors are continuous.)**

Input Feature	Range
$N_b^*$	2, 3, 4, 5
$R$	[6 in, 12 in]
$\Omega$	[3000 RPM, 6000 RPM]
$\theta_{tw}$	$[-20^\circ, 0^\circ]$
$TR$	[1, 3]
$c_{tip}$	[0.5 in, 1.5 in]
$\theta_0$	$[0^\circ, +10^\circ]$
$M$	[0%, 10%]
$t/c$	[6%, 15%]

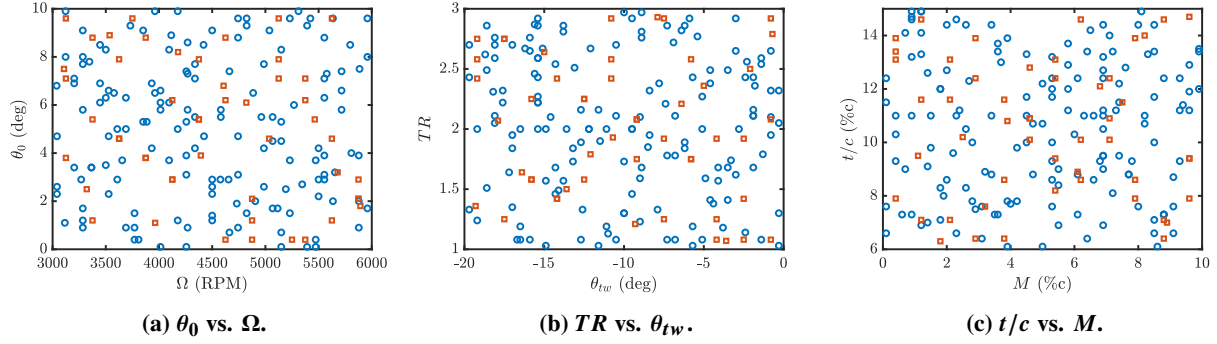


**Fig. 2** Training and test datasets projected on a 2-D input subspace of the input feature space (blue circles are training data and orange squares are test data).

The low-fidelity tools discussed in the subsequent section were then used to simulate the data points prescribed by each input feature space, and the two modeling methodologies were used to create aerodynamic and aeroacoustic prediction models with functional relationships to the defined input features.

## B. Low-Fidelity Tools

Throughout this work, various low-fidelity tools were utilized to allow for rotor designs comprised of the NACA four-digit airfoil geometric parameters:  $M$  and  $t/c$ , as well as characteristic rotor properties such as  $N_b$ ,  $R$ ,  $\Omega$ ,  $\theta_{tw}$ ,  $TR$ ,  $c_{tip}$ , and  $\theta_0$ . Previous work done by the main author in Ref. [13] used an analytical expression to define the twist distribution,  $\theta(r)$ , which had a functional dependence on a target thrust value,  $C_{T_{design}}$ , calculated a priori. Since  $C_{T_{design}}$  is calculated using various rotor properties, the inputs from this previous work were highly coupled, with the variation of rotor properties directly affecting  $\theta(r)$ . In an effort to decouple the inputs to provide a direct comparison of their effect on the prediction output, a linear twist distribution was used in this work:

$$\theta(r) = \theta_0 + \theta_{tw}(r - 0.75), \quad (2)$$

where  $\theta_0$  is measured at  $0.75R$ .

The Comprehensive Analytical Model of Rotorcraft Aerodynamics and Dynamics (CAMRAD II) [23] was used to model rotor aerodynamics at each design point in the DoE input feature spaces. CAMRAD II is a comprehensive rotorcraft analysis code, allowing for the use of different wake models (e.g., uniform inflow, prescribed wake, and free wake) and different blade dynamics (e.g., rigid and elastic). CAMRAD II requires aerodynamic airfoil coefficient data, which can either be generated using analytical equations or can be supplied by the user in the form of an airfoil table.

CAMRAD II was used in this work with a uniform inflow model, which significantly reduced computational cost associated with dataset generation when compared to using a free wake model. It should be noted that the use of a uniform inflow model rather than a free wake model could have aerodynamic and aeroacoustic implications [11]; however, since the goal of this study was prediction model comparison, any potential differences were deemed acceptable for this work. All rotors in this work were also assumed to have rigid (i.e., nondeforming) blades since elastic blade properties are not currently known.

Airfoil tables in the C81 format were generated at each data point in the input feature spaces using the structured, unsteady Reynolds-averaged Navier-Stokes solver, OVERFLOW2 [24]. Two-dimensional, steady-state OVERFLOW2 simulations were conducted over a range of angles of attack,  $\alpha$ , and freestream Mach numbers,  $M_\infty$ , using the improved Einfeldt's version of the second-order spatial Harten, Lax, and van Leer (HLLE++) upwind scheme [25] coupled with the one equation Spalart-Allmaras (SA-neg-noft2) turbulence model and the Medida-Baeder  $\gamma - Re_\theta - SA$  transition model [26]. Values of  $\alpha$  ranged from  $-22^\circ \leq \alpha \leq +22^\circ$ , and  $M_\infty$  values ranged from  $0.1 \leq M_\infty \leq 0.6$ . A chord-based reference Reynolds number,  $Re_{ref}$ , of 500,000 was prescribed, which was scaled by the  $M_\infty$  value correspondent to each simulation. A preexisting C81 table generated for an NACA 0012 airfoil profile was used as a template and cubic interpolation was utilized to combine the airfoil coefficient data calculated using OVERFLOW2 with the preexisting template over the specified range of  $\alpha$  and  $M_\infty$  values. This computational strategy was determined by Boyd et al. [27] to be effective at capturing low  $Re$  effects associated with sUAS-sized rotors.

The C81 table data were used by CAMRAD II for predicting spanwise aerodynamic forces and moments, which were then integrated over the entirety of the rotor to produce rotor thrust,  $T_{pred}$ , power,  $P_{pred}$ , and torque,  $Q_{pred}$ . Because rotor power and torque are related via the relationship:  $P = \Omega Q$ , only  $T_{pred}$  and  $P_{pred}$  were used for subsequent aerodynamic prediction modeling. The ANOPP2 Aeroacoustic Rotor Noise (AARON) tool was then used to propagate the tonal acoustics to an arc of observer locations  $15R$  away from the center of the rotor using Farassat's formulation 1A (F1A) [28] of the FW-H acoustic analogy under a compact-chord assumption [29] for both the loading and thickness tonal noise terms. Other sectional blade quantities, such as the induced flow velocity and effective angle of attack,  $\alpha_{eff}$ , were also used by AARON to calculate the broadband self-noise at the same observer locations using an implementation of the BPM semiempirical methodology [9]. It should be noted that the BPM method accounted for the zero-lift angle of attack,  $\alpha_0$ , of each airfoil in the input feature spaces and the blades were treated as fully turbulent (i.e., trip setting of 1), which neglected laminar boundary layer vortex shedding (LBL-VS) noise. Though this LBL-VS noise was shown to be prominent for smooth sUAS-sized blades by Thurman et al. [6, 7], further research toward implementation of LBL-VS noise in the BPM method is necessary for accurate predictions so it was neglected in this work. The thickness ( $SPL_{th}$ ) and loading ( $SPL_{lo}$ ) components of the tonal noise at the fundamental BPF of each respective rotor were used for the subsequent prediction modeling effort along with a broadband noise overall sound pressure level,  $OASPL_{BB}$ , calculated over the predicted broadband frequency range.

Using these two aerodynamic quantities,  $T_{pred}$  and  $P_{pred}$ , and three aeroacoustic quantities,  $SPL_{th}$ ,  $SPL_{lo}$ , and  $OASPL_{BB}$  calculated at 13 observers located  $15R$  away from the center of the rotor at observer angles,  $\Theta_{obs}$ , ranging from  $-90^\circ \leq \Theta_{obs} \leq +90^\circ$  (i.e.,  $\Delta\Theta_{obs} = 15^\circ$  with  $\Theta_{obs} = -90^\circ$  corresponding to an observer located directly below the center of the rotor), a total of 5 and 41 prediction models were created using the ANN and MOF modeling strategies, respectively. The reduced number of ANN prediction models was the result of using a multioutput strategy described in Section III.C.1.

## C. Prediction Modeling Methodologies

### 1. Artificial Neural Network Modeling

ANNs were selected as a candidate prediction model type to fit the data within the input feature space based on their successful implementation in previous work [13, 14]. ANNs aim to replicate the architecture of the neurons in the human brain, set up in layers as shown in Fig. 3. Each ‘‘hidden’’ layer consists of a number of neurons, represented by circles in Fig. 3, aligned in parallel. All neurons of a particular layer are activated in unison, with different multiplicative weights along the connections between neurons, inputs, and outputs. In general if an ANN has more than one hidden layer, it is considered a multilayer perceptron (MLP); otherwise, it is a single-layer perceptron (SLP).

In the case of the two-layer MLP shown in Fig. 3, the general equations defining the ANN are:

$$z_{1h} = \gamma_1 \left( \sum_{k=1}^s \omega_{hk} \mathbf{x}_k + \omega_{h0} \right), \quad (3)$$

$$z_{2p} = \gamma_2 \left( \sum_{h=1}^H \omega_{ph} z_{1h} + \omega_{p0} \right), \quad (4)$$

$$f_j(\mathbf{x}_k, \mathbf{x}_{k+1}, \dots, \mathbf{x}_s) = \gamma_3 \left( \sum_{p=1}^P \mu_p z_{2p} + \mu_0 \right) = \hat{\mathbf{y}}_j, \quad (5)$$

where  $s$  is the number of input features,  $H$  is the number of neurons in the first hidden layer, and  $P$  is the number of neurons in the second hidden layer. In Eq. (3),  $\gamma$  is the activation function used by the neurons in a hidden or output layer,  $z$  is the output from a neuron in a hidden layer,  $\omega_{hk}$  are the weights between the input features and the first hidden layer,  $\omega_{ph}$  are the weights between the first and second hidden layers,  $\mu_p$  are the weights between the second hidden layer and the output,  $\omega_0$  and  $\mu_0$  are commonly used bias terms (i.e., intercepts) added to each hidden layer, and  $f_j$  is the  $j^{\text{th}}$  ANN model producing the predicted values,  $\hat{\mathbf{y}}_j$ .

The activation functions,  $\gamma$ , can be thought of as functional ‘mappings’ of a neuron’s input onto highly nonlinear hyperplanes defined by the structure of  $\gamma$ . These activation functions are necessary to introduce nonlinearity to the ANN, enabling it to effectively model complex, nonlinear input-output relationships.

The training procedure for an ANN first involves the random initialization of all weights along the connections between neurons, inputs and outputs. The input data,  $(\mathbf{x}_k, \mathbf{x}_{k+1}, \dots, \mathbf{x}_s)$ , are then provided to the ANN in a feedforward

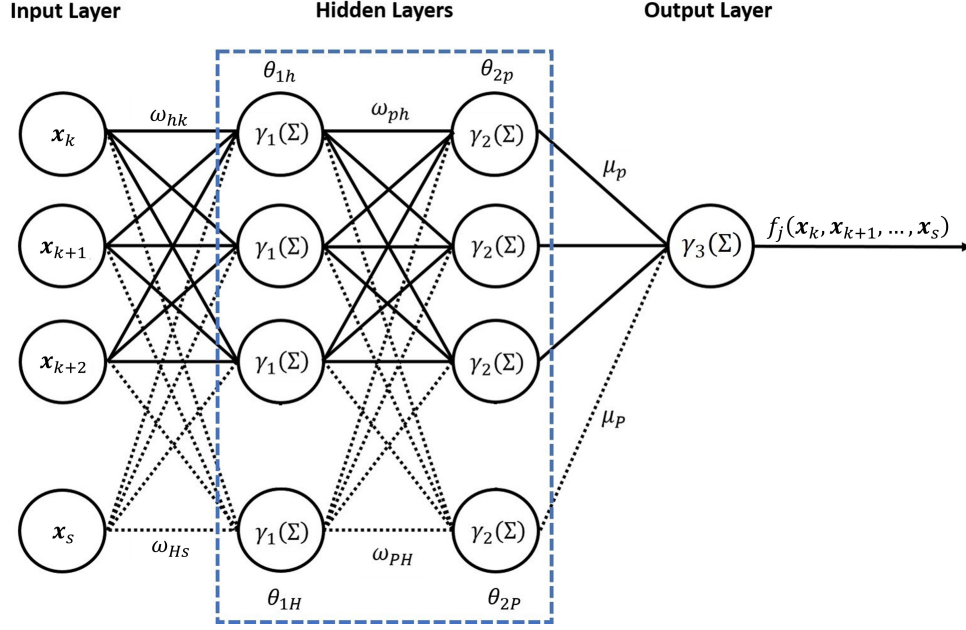


Fig. 3 Illustration of an MLP. Adapted from Thurman [14].

manner and predicted values,  $\hat{y}_j$ , are produced. These predicted values are then tested against the provided output, or labeled, data associated with the input data, and a cost function,  $\tilde{E}$ , is evaluated. This cost function is a numerical description of the error between the labeled output data,  $y_j$ , and the predicted output,  $\hat{y}_j$ . The error calculated by the cost function is then propagated from the output,  $\hat{y}_j$ , back through the ANN via the chain rule of differentiation:

$$\frac{\partial \tilde{E}}{\partial \omega_{hk}} = \frac{\partial \tilde{E}}{\partial \hat{y}_j} \frac{\partial \hat{y}_j}{\partial z_{2h}} \frac{\partial z_{2h}}{\partial \omega_{ph}} \frac{\partial \omega_{ph}}{\partial z_{1h}} \frac{\partial z_{1h}}{\partial \omega_{hk}}, \quad (6)$$

where  $\partial \tilde{E} / \partial \omega_{hk}$  is the change in error associated with changing the value of the weight,  $\omega_{hk}$ , between the input layer and the first hidden layer for the two-layer MLP shown in Fig. 3. This method for propagating the error back through the ANN has been coined *backpropagation* by Rumelhart et al. [30]. The gradients calculated using this backpropagation are typically used with an optimization algorithm to update the weights along each connection in the ANN. One optimization cycle through the training data samples,  $N$ , is considered to be one *epoch*. Various forms of regularization are often used in the ANN training process to promote optimization convergence and to help prevent the trained model from overfitting the input data.

In general, there are a multitude of different ANN model architectures (number of hidden layers, number of neurons per hidden layer, type of activation function used, etc.), regularization techniques (data scaling,  $L_1$  or  $L_2$  regularization, early stopping, etc.), and hyperparameters that can be used to generate accurate prediction models. These elements of the ANN modeling procedure are typically determined heuristically and are problem specific, varying with the input-output relationship being modeled. In other words, the optimal ANN structure used for one problem may be different from the ANN structure of another. Because of these potential ANN model form variations as well as the common difficulties associated with creating ANNs, the NASA code, the ANOPP2 Artificial Neural Network Tool (AANNT) [31], was utilized in this work for prediction model development, deployment, and model sensitivity analyses. The reader is referred to Refs. [14] and [31] for more details on the usage and applicability of AANNT.

The prediction model development portion of AANNT was first used to rescale the continuous input features in the input feature space using:

$$\tilde{\mathbf{x}}_k = \frac{\mathbf{x}_k - \mathbf{x}_{k_{min}}}{\mathbf{x}_{k_{max}} - \mathbf{x}_{k_{min}}}, \quad (7)$$

where the subscript,  $k$ , corresponds to the number of input features. In Eq. (7),  $\tilde{\mathbf{x}}$  denotes a rescaled input feature,  $\mathbf{x}$ , ranging from  $0 \leq \tilde{\mathbf{x}} \leq 1$ . One-hot encoding was used for  $N_b$  since it was a categorical input feature. This process of

one-hot encoding generates additional binary input features correspondent to the discrete values associated with  $N_b$  (i.e.,  $N_b = 2, N_b = 3, N_b = 4$ , or  $N_b = 5$ ).

Once the data were rescaled, the grid search functionality of AANNT was used to explore various model architectures, which included various combinations of hidden layer activation functions, output layer activation functions, number of neurons in the hidden layers, loss functions used by the optimizer, and various types of regularization (e.g.,  $L_1$ ,  $L_2$ , and dropout or randomly eliminating a certain percentage of the neurons in the hidden layer during each epoch of the optimization procedure). The hidden layer activation functions tested in the grid search procedure were GELU [32] and Swish [33]. ANN architectures including one and two hidden layers consisting of 25, 50, and 100 neurons were also tested in the grid search. The HUBER [34] loss function, which is a combination of the mean absolute error and mean squared error loss functions, was used for model training. Various amounts of regularization were tested in the grid search including dropout rates of 0 and 25%, as well as  $L_1$  and  $L_2$  regularization values of 0.0, 0.01, and 0.1. All models were trained over 1000 epochs using the adaptive moment estimation (ADAM) optimizer [35], and an early stopping criterion was used, which terminated the training procedure if there was no improvement of  $\bar{E}$  after 150 epochs. A table summarizing the different model parameters used in the grid search is provided in Table 2.

**Table 2 Model parameters explored with AANNT grid search.**

Hyperparameter	Values
Number of Hidden Layers	1, 2
Number of Neurons in each Hidden Layer	25, 50, 100
Hidden Layer Activation Functions	GELU, Swish
Output Layer Activation Functions	linear, GELU, Swish
Loss Function	HUBER
Dropout Rates	0, 25%
$L_1$ Regularization	0.0, 0.01, 0.1
$L_2$ Regularization	0.0, 0.01, 0.1

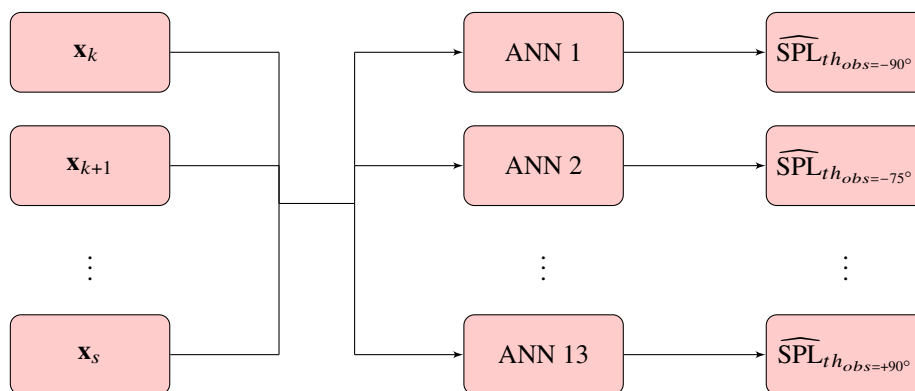


**Fig. 4 Illustration of the multioutput model architecture for the  $SPL_{th}$  ANN.**

The grid search procedure implemented in AANNT using the various model parameters shown in Table 2 was used for each of the prediction models developed in this work, and the ANN models with the best prediction performance evaluated over the test data (previously unseen by the model) were selected as the final ANN models. It should be noted that using test data for optimal model selection introduces model dependency on these data; however, model evaluation over test data is necessary to ensure the models are not overfitted to the training data. The multioutput functionality of AANNT was used for each of the three aeroacoustic metrics to train models capable of prediction at each of the 13 observer locations rather than the two alternatives: training a separate prediction model for each observer location or including the observer location as an input feature. Training a separate prediction model for each observer location

would have greatly increased the total time required to train all models, whereas including the observer location as an input could possibly skew prediction model dependency toward its influence, since the input feature space was uniform with respect to all other input variables. The current multioutput implementation in AANNT trains a separate model for each output in parallel, using the same hyperparameters for each of the trained models. An illustration of the multioutput model architecture for the  $\widehat{\text{SPL}}_{th}$  ANN is shown in Fig. 4 where the hat symbol denotes a quantity predicted by the ANN. The optimal model architecture and training regularization identified by AANNT for each output are shown in Tables 3 and 4, respectively.

**Table 3 Optimal ANN architecture.**

Model	Number of Hidden Layers	Number of Neurons in Each Hidden Layer	Hidden Layer Activation Function	Output Layer Activation Function
$T_{pred}$	2	50	Swish	Swish
$P_{pred}$	2	50	Swish	Swish
$\widehat{\text{SPL}}_{th}$	1	100	Swish	Linear
$\widehat{\text{SPL}}_{lo}$	1	50	GELU	Linear
$\text{OASPL}_{BB}$	1	50	Swish	Linear

**Table 4 Optimal regularization used to train ANNs.**

Model	Dropout Rate	$L_1$ Regularization	$L_2$ Regularization
$T_{pred}$	0	0	0
$P_{pred}$	0	0	0.1
$\widehat{\text{SPL}}_{th}$	0	0	0
$\widehat{\text{SPL}}_{lo}$	0	0.1	0
$\text{OASPL}_{BB}$	0	0.01	0.1

## 2. Multivariate Orthogonal Function Modeling

Challenges for computational experiment model structure selection arise because the response data have no random error, which means that modeling residuals are derived only from modeling error. Although the parameter estimates obtained from least-squares regression are still valid, the parameter standard errors, parameter confidence intervals, parameter significance testing, and model prediction intervals lack statistical justification. This complicates the use of model structure determination methods that rely on significance testing, such as stepwise regression. MOF modeling, described in Refs. [36] and [37], was selected as the algorithm to determine which model terms to include in the polynomial structure. The MOF model structure determination method does not rely on significance testing and instead selects regressors to include in the model based on their independent ability to improve characterization of the response variable.

The MOF modeling approach is initiated by orthogonalizing a predefined set of candidate regressors using an algorithm such as Gram-Schmidt orthogonalization or QR decomposition. Orthogonal regressors are convenient for model structure development because of the ability to independently assess the candidate regressors potential to model the response variable—this facilitates only including model terms that significantly contribute to model effectiveness. Upon orthogonalization of candidate regressors, the least-squares regression equation is

$$\mathbf{y}_j = \mathbf{P}\mathbf{a} + \mathbf{v}, \quad (8)$$

where  $\mathbf{P}$  is an  $N \times n_p$  matrix consisting of column vectors holding orthogonal regressors,  $\mathbf{p}_l$ , from  $l = 1, 2, \dots, n_p$  and  $\mathbf{a}$  is a vector of  $n_p$  unknown parameters. For least-squares parameter estimation, the optimal estimate of the unknown

parameters  $\mathbf{a}$  is determined by minimizing the cost function:

$$J(\mathbf{a}) = \frac{1}{2} (\mathbf{y}_j - \mathbf{P}\mathbf{a})^T (\mathbf{y}_j - \mathbf{P}\mathbf{a}). \quad (9)$$

It follows that the solution to compute an optimal estimate of the unknown parameters is

$$\hat{\mathbf{a}} = (\mathbf{P}^T \mathbf{P})^{-1} \mathbf{P}^T \mathbf{y}_j, \quad (10)$$

where  $\hat{\mathbf{a}}$  is a vector of  $n_p$  estimated parameters. Because the matrix  $\mathbf{P}^T \mathbf{P}$  is diagonal due to the mutual orthogonality of the regressors, the least-squares estimate for the  $l^{\text{th}}$  parameter decouples and takes the form:

$$\hat{a}_l = \frac{\mathbf{p}_l^T \mathbf{y}_j}{\mathbf{p}_l^T \mathbf{p}_l} \quad (11)$$

to obtain a vector of estimated parameters,  $\hat{\mathbf{a}} = [\hat{a}_1, \hat{a}_2, \dots, \hat{a}_{n_p}]^T$ . It follows that the least-squares cost function can be rewritten as:

$$J(\hat{\mathbf{a}}) = \frac{1}{2} \left( \mathbf{y}_j^T \mathbf{y}_j - \sum_{l=1}^{n_p} \frac{(\mathbf{p}_l^T \mathbf{y}_j)^2}{\mathbf{p}_l^T \mathbf{p}_l} \right), \quad (12)$$

which highlights the fact that the contribution of each orthogonal regressor to improve the least-squares model fit can be assessed independently from other orthogonal regressors in a particular model structure. This allows a model structure to be identified without iteration [37].

Using the above developments, the regressors are ranked from highest to lowest decrease in the mean squared fit error (MSFE), which is reflected by the  $\frac{(\mathbf{p}_l^T \mathbf{y}_j)^2}{\mathbf{p}_l^T \mathbf{p}_l}$  term for each regressor in Eq. (12). In other words, this ranks the regressors from highest to lowest ability to improve the model. Candidate regressors are brought into the model structure in this order. Deciding which terms to include in the final model can then be done in consultation with one or more statistical metrics. The most common threshold for MOF modeling is to minimize the predicted squared error (PSE) [37, 38]. The PSE is the sum of the MSFE for a model and a complexity penalty term related to the number of terms included in the model

$$\text{PSE} = \frac{1}{N} (\mathbf{y}_j - \mathbf{P}\hat{\mathbf{a}})^T (\mathbf{y}_j - \mathbf{P}\hat{\mathbf{a}}) + \sigma_{\max}^2 \frac{p}{N}, \quad (13)$$

where  $p$  is the number of terms in the current model structure and  $\sigma_{\max}^2$  is an estimate of the upper-bound of mean squared error for the model prediction of data not used to develop the model. In physical testing, the quantity  $\sigma_{\max}^2$  can be estimated using the variance of measured responses between repeated data points or from the variance between the measured response,  $\mathbf{y}_j$ , and mean measured response,  $\bar{\mathbf{y}}_j$ . In the present application where the response of repeat points is identical, the latter approach is used to provide an estimate of  $\sigma_{\max}^2$  as:

$$\sigma_{\max}^2 = \frac{1}{N-1} \sum_{i=1}^N [\mathbf{y}_j(i) - \bar{\mathbf{y}}_j]^2. \quad (14)$$

When the orthogonalized regressors are ranked as stated above, the PSE metric is guaranteed to have a single global minimum [37].

Another statistical metric that can be used as a stopping criterion for MOF modeling is the coefficient of determination,  $R_d^2$  [18, 39, 40], where the subscript  $d$  is used here to avoid confusion with rotor radius,  $R$ . The  $R_d^2$  metric quantifies the model fit by characterizing the amount of variation of the response variable about its mean that is described by the model. Using the orthogonal regressors, the  $R_d^2$  metric is calculated as:

$$R_d^2 = \frac{\hat{\mathbf{a}}^T \mathbf{P}^T \mathbf{y}_j - N \bar{\mathbf{y}}_j^2}{\mathbf{y}_j^T \mathbf{y}_j - N \bar{\mathbf{y}}_j^2}. \quad (15)$$

The  $R_d^2$  metric will always increase with addition of new orthogonalized model terms. Consequently, it is important that each model term added on the basis of the  $R_d^2$  metric significantly increases its value. A common  $R_d^2$  increase

constituting a significant increase with the addition of a new model term is  $\Delta R_d^2 = 0.5\%$  [37]. This means that the model term describes a minimum of 0.5% of the total variation about the mean response.

Both PSE and  $R_d^2$  were used as a cutoff threshold for candidate model terms to include in the final model structure. Once the orthogonal regressors were ranked by their ability to reduce the MSFE, the cutoff for model term addition was chosen to be either the candidate model term that minimized the PSE or the last term to increase  $R_d^2$  by 0.5%, whichever admitted more terms into the model. MOF modeling has been successfully used in previous modeling studies using designed experiments for fixed-wing aircraft [41, 42], propellers at incidence [43], and computational experiments for an eVTOL aircraft [17].

After determining the model terms to include in the model structure, the final parameter values were estimated using ordinary least-squares regression in ordinary regressor space. The software implementing the MOF modeling and least-squares regression algorithm was from the System IDentification Programs for AirCRAFT (SIDPAC) software toolbox [44]. Separate models were created for the two aerodynamic quantities,  $T_{pred}$  and  $P_{pred}$ , as well as for the three aeroacoustic quantities,  $SPL_{th}$ ,  $SPL_{lo}$ , and  $OASPL_{BB}$ , evaluated at each of the observer locations for a total of 41 prediction models.

## IV. Results

### A. Prediction Model Performance and Validation

ANN and MOF prediction models were trained over the  $T_{pred}$ ,  $P_{pred}$ ,  $SPL_{th}$ ,  $SPL_{lo}$ , and  $OASPL_{BB}$  output data and the normalized mean absolute error (NMAE) metric,

$$\text{NMAE} = 100 \times \frac{1}{\text{range}(\mathbf{y}_j)} \frac{1}{N} \sum_{i=1}^N |y_j^i - \hat{y}_j^i|, \quad (16)$$

and normalized root mean squared error (NRMSE) metric,

$$\text{NRMSE} = 100 \times \frac{1}{\text{range}(\mathbf{y}_j)} \sqrt{\frac{1}{N} \sum_{i=1}^N (y_j^i - \hat{y}_j^i)^2}, \quad (17)$$

were evaluated over both the training and test data, which can be seen in Tables 5 and 6.

**Table 5** ANN model error metrics evaluated over the training and test data (all expressed as a percentage). (\* indicates average over 13 observer locations.)

Metric	$T_{pred}$	$P_{pred}$	$SPL_{th}^*$	$SPL_{lo}^*$	$OASPL_{BB}^*$
$\text{NMAE}_{\text{train}}$	0.307	1.29	1.35	1.92	0.849
$\text{NMAE}_{\text{test}}$	1.35	1.22	2.42	3.11	2.55
$\text{NRMSE}_{\text{train}}$	0.420	2.17	2.04	3.24	1.12
$\text{NRMSE}_{\text{test}}$	2.40	2.18	3.27	4.32	3.22

**Table 6** MOF model error metrics evaluated over the training and test data (all expressed as a percentage). (\* indicates average over 13 observer locations.)

Metric	$T_{pred}$	$P_{pred}$	$SPL_{th}^*$	$SPL_{lo}^*$	$OASPL_{BB}^*$
$\text{NMAE}_{\text{train}}$	1.76	1.95	2.83	3.43	2.65
$\text{NMAE}_{\text{test}}$	1.79	1.61	3.76	4.10	4.39
$\text{NRMSE}_{\text{train}}$	3.05	3.85	3.59	4.57	3.34
$\text{NRMSE}_{\text{test}}$	3.22	2.71	4.88	5.34	5.25

The normalization of these two error metrics allows for a better quantitative comparison between different prediction models, which in general, could have been created over training datasets with differing scales (e.g., Newtons vs. decibels). Since models were trained for the three aeroacoustic metrics at each of the 13 observer locations, an average of the NMAE and NRMSE values over all observer locations was taken for  $\widehat{SPL}_{lo}$ ,  $\widehat{SPL}_{th}$ , and  $\widehat{OASPL}_{BB}$ .

Tables 5 and 6 show that the ANN prediction models have lower modeling and prediction error compared to the MOF models for all aerodynamic and aeroacoustic quantities. However, in general, it can be said that all ANN and MOF models in this work exhibit excellent accuracy over the test data (previously unseen by the models), demonstrating their ability to both generalize well over new data and adequately represent the entirety of the input feature space. Since the NRMSE metric imposes a larger weight on residual outliers, its small increase when compared to the NMAE for all prediction models indicates that there are no significant prediction outliers. The small difference in the modeling error when compared to the prediction error for both the ANN and MOF models also suggests that these models did not overfit the training data.

To further validate the models and provide a qualitative comparison, the test data point with the furthest average Euclidean distance from training data points was selected to compare results predicted using both the ANN and MOF models against results generated using the low-fidelity tools. The value of each input feature for the test data point are:  $N_b = 5$ ,  $R = 10.1$  in,  $\Omega = 5893$  RPM,  $\theta_{tw} = -13.6^\circ$ ,  $TR = 1.5$ ,  $c_{tip} = 0.68$  in,  $\theta_0 = 1.8^\circ$ ,  $M = 0.4\%c$ , and  $t/c = 13.4\%c$ . Because this test data point was furthest away from the training data used for model development, it provides a good, concise demonstration of the prediction capabilities of the models. The aerodynamic results generated using the low-fidelity tools at this point are  $T_{pred} = 1.58$  lb and  $P_{pred} = 0.273$  HP, the predicted results using the ANN models are  $\hat{T}_{pred} = 2.01$  lb and  $\hat{P}_{pred} = 0.284$  HP, and the predicted results using the MOF models are  $\hat{T}_{pred} = 2.08$  lb and  $\hat{P}_{pred} = 0.281$  HP. A comparison of the predicted aeroacoustic results is shown in Fig. 5. It should be noted that the aeroacoustic results in Fig. 5 were mirrored about the axis of rotation due to azimuthal symmetry. As can be seen from Figs. 5a and 5c, both the ANN and MOF models exhibit excellent agreement with the results generated using the low-fidelity tools for both the tonal thickness and broadband noise with the MOF models slightly overpredicting and the ANN models slightly underpredicting  $\widehat{SPL}_{th}$ , respectively. The loading noise directivity comparison in Fig. 5b shows that both prediction models mispredict the trend seen in the low-fidelity results, with the ANN model having better agreement below the rotor plane and the MOF models having better agreement above the rotor plane. Another observation made from the thickness and loading noise directivity plots shown in Figs. 5a and 5b is that there is a null region directly above and below the rotor (i.e.,  $\Theta_{obs} = +90^\circ$  and  $\Theta_{obs} = -90^\circ$ ). This null region in the tonal noise is known to occur for isolated hovering rotors and is due to the azimuthal symmetry of the tonal noise signature about the axis of rotation. Though the tonal noise has no contribution above or below the rotor, which produces large negative  $\widehat{SPL}_{th}$  and  $\widehat{SPL}_{lo}$  values, there is high variance in the training and test data at these observer locations.

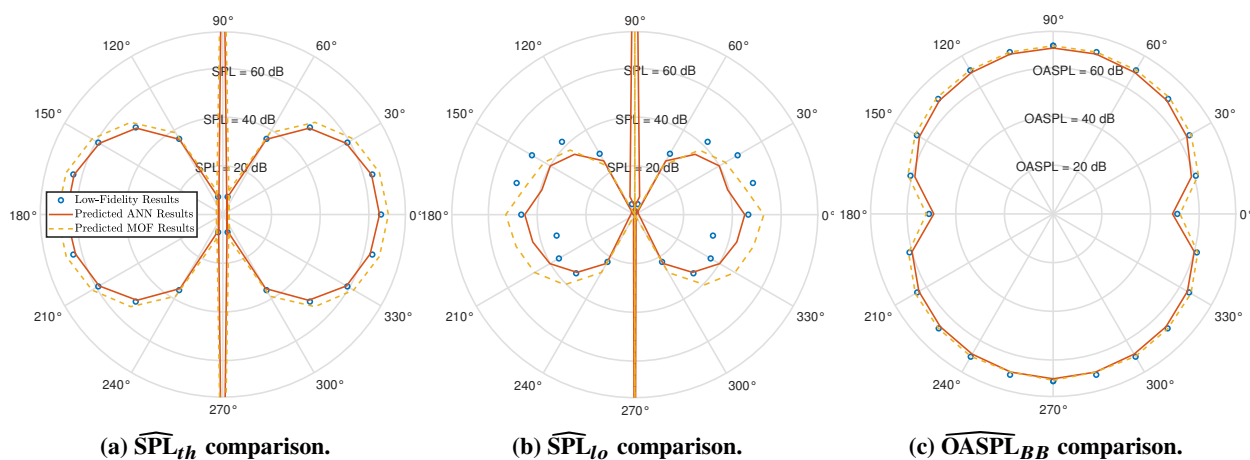


**Fig. 5** Acoustic directivities at the test data point with the furthest average Euclidean distance from the training data. The input feature values correspondent to this point are:  $N_b = 5$ ,  $R = 10.1$  in,  $\Omega = 5893$  RPM,  $\theta_{tw} = -13.6^\circ$ ,  $TR = 1.5$ ,  $c_{tip} = 0.68$  in,  $\theta_0 = 1.8^\circ$ ,  $M = 0.4\%c$ , and  $t/c = 13.4\%c$ .

To further investigate each model's prediction error for these two tonal aeroacoustic quantities, the training and test NMAE and NRMSE values at each observer location are shown in Figs. 6 and 7, respectively. Similar figures for

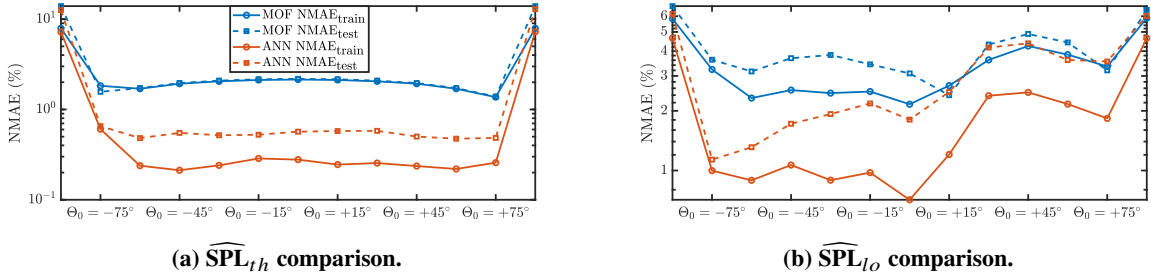


Fig. 6 NMAE values for  $\widehat{SPL}$  at all observer locations.

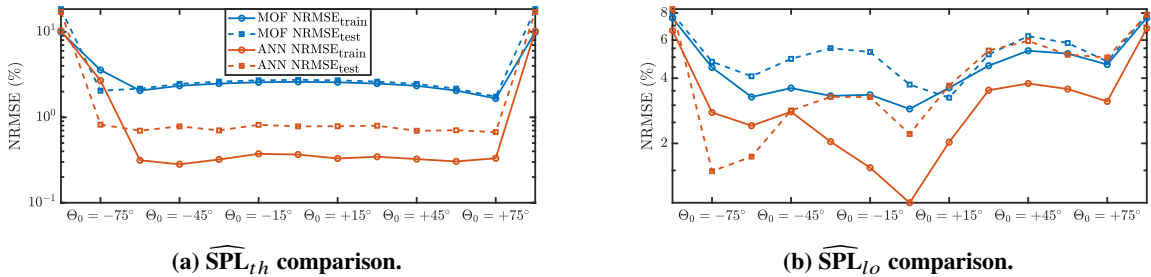


Fig. 7 NRMSE values for  $\widehat{SPL}$  at all observer locations.

$\widehat{OASPL}_{BB}$  are not included because there is no null region in the broadband noise directivity, as shown in Fig. 5c. It can be seen in Figs. 6 and 7 that both the ANN and MOF models have larger error values at observers located directly above and below the rotor, with the ANN models having slightly less error at all other observer locations for  $\widehat{SPL}_{th}$ . The highly nonlinear acoustic directivity pattern of  $\widehat{SPL}_{lo}$  shown in Fig. 5 also degrades the predictive ability of both the ANN and MOF models when compared to the NMAE and NRMSE results for  $\widehat{SPL}_{th}$  shown in Figs. 6a and 7a. Although the prediction error is larger directly above and below the rotor, the ANN and MOF models still exhibit NMAE and NRMSE values less than 15%, exemplifying their capacity for modeling highly nonlinear functional relationships.

## B. Aerodynamic and Aeroacoustic Characterization

To compare the effects of each input feature on the rotor aerodynamics and aeroacoustics, model-independent sensitivity analyses were performed using the sensitivity analysis portion of AANNT. The method of Sobol' was selected for this work, which used a Saltelli [45] sample space consisting of 40,960 samples. In general, model-independent forms of sensitivity analysis can be dependent on the size of the sample space and the predictive precision of the model. It was shown in Thurman [14] through increasing the number of samples in the sensitivity analysis, that 40,960 samples produced results that were invariant to the size of the sample space. Though the Sobol' sensitivity analysis calculates first-, second-, and total sensitivity results for each input feature, only the total sensitivity metrics were used for brevity. These total sensitivity results can be compared to infer which input feature, including its interactions with other input features, is most significant to the prediction model (i.e., largest sensitivity index). It should be noted that the regressor ranking procedure involved in MOF modeling, as well as the magnitude of the coefficients for each regression model term, provide insight as to which input features and input feature interactions are significant to the model. The complex ANN architecture obscures any sort of input feature ranking from the model form and because of this, the Sobol' sensitivity analysis was performed over both the ANN and MOF models to ensure that both model types produce similar insight regarding the importance of each input feature.

Total sensitivity indices for the aerodynamic (i.e.,  $\hat{T}_{pred}$  and  $\hat{P}_{pred}$ ) ANN and MOF models are shown in Fig. 8. It can be seen that both model types exhibit similar sensitivity results in terms of feature ranking, indicating that both model types represent the underlying physical relationship between the input features and aerodynamic outputs in a similar way. It can be ascertained from Fig. 8 that both  $\hat{T}_{pred}$  and  $\hat{P}_{pred}$  have the largest dependency on  $R$ , followed by  $\theta_0$  for  $\hat{T}_{pred}$  and  $\Omega$  for  $\hat{P}_{pred}$ , respectively. These results are intuitive and should be expected for dimensional isolated hovering rotor aerodynamics since power has an additional dependency on  $\Omega R$  when compared to thrust and

since  $\theta_0$  serves to directly increase the sectional angle of attack,  $\alpha$ . The investigation of dimensionless aerodynamic coefficients like the thrust coefficient,  $C_T$ , and power coefficient,  $C_P$ , was not considered because these coefficients can hold identical values for changing input parameters (e.g.,  $C_T = \frac{T}{\rho\pi R^2(\Omega R)^2}$ ). It should be noted, however, that when considering dimensionless aerodynamic coefficients, the  $R$  dependency of  $C_T$  and  $C_P$  would be negligible and the dependency on  $\Omega$  may still be significant (although of lesser importance from other input features) due to potential low  $Re$  effects associated with sUAS rotors [27].

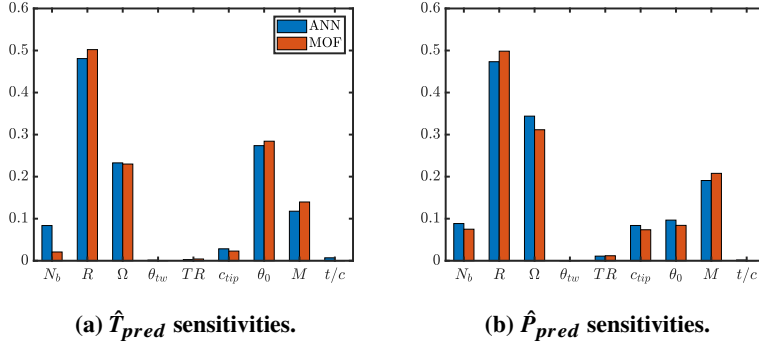


**Fig. 8** Aerodynamic Sobol' sensitivity indices for the ANN and MOF model types.

Sensitivity analysis results for the aeroacoustic quantities,  $\widehat{SPL}_{th}$ ,  $\widehat{SPL}_{lo}$ , and  $\widehat{OASPL}_{BB}$  are shown in Fig. 9. Since in general, tonal noise (i.e., thickness and loading) is dominant in the rotor plane (i.e.,  $\Theta_{obs} = 0^\circ$ ), the tonal noise sensitivity indices in Figs. 9a and 9b are only shown at  $\Theta_{obs} = 0^\circ$ . Likewise, broadband self-noise has an out-of-plane dominance as illustrated in Fig. 5, so the sensitivities in Fig. 9c are shown at  $\Theta_{obs} = -90^\circ$ . Again, it can be seen that both model types exhibit similar sensitivity results in terms of feature ranking. It can also be seen that  $\Omega$  has the largest influence on all three aeroacoustic quantities followed by  $R$ . Although changes to both  $\Omega$  and  $R$  would modify sectional aerodynamic quantities, these two input features also serve a fundamental role in the acoustic F1A [28] calculation via the Doppler factor (i.e.,  $1 - M_r$ , where  $M_r$  is the Mach number in the radiated direction), explaining their significance to both  $\widehat{SPL}_{th}$  and  $\widehat{SPL}_{lo}$ .

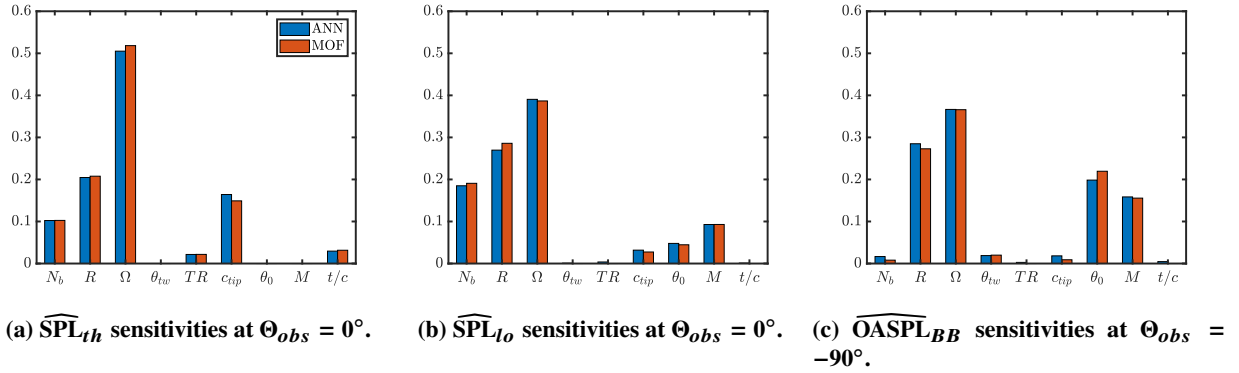


**Fig. 9** Aeroacoustic Sobol' sensitivity indices for the ANN and MOF model types.

It is interesting to note the small influence of  $t/c$  on  $\widehat{SPL}_{th}$ , considering this is a fundamental term in the compact-chord assumption [29] of the F1A equation. This may be explained by the dimensionless form of  $t/c$ . Increasing the *dimensional* chord thickness would increase the fluid displacement caused by the rotor (i.e.,  $\widehat{SPL}_{th}$ ), possibly elucidating the large sensitivity of  $\widehat{SPL}_{th}$  to  $c_{tip}$  when compared to  $t/c$ . Since the broadband self-noise modeled by the BPM method implemented by AARON is highly dependent on boundary layer turbulence, the large influence of  $\Omega$  and  $R$  on  $\widehat{OASPL}_{BB}$  shown in Fig. 9c makes sense because these two input features influence the spanwise Reynolds number,  $Re = \frac{\Omega R c}{\nu}$ . Because of this  $Re$  dependency, it was expected that  $c_{tip}$  would also have a large influence on  $\widehat{OASPL}_{BB}$ ; however, the range and magnitude of  $c_{tip}$  (i.e., [0.5 in, 1.5 in]) are much smaller than for  $\Omega$  and  $R$ , mitigating

its effectiveness when considering  $Re$ . Based upon the results in Fig. 9c, it can be said that even mild trailing edge boundary layer separation caused by  $\theta_0$  or  $M$  has a larger effect on the broadband self-noise than  $c_{tip}$ .

### C. Discussion

Although the MOF prediction results are not as accurate as the ANN results for this study, MOF has the benefits of model training only taking a few seconds and models that can be written explicitly in a compact polynomial equation that is easy to evaluate for making predictions. ANN models are better at conforming to nonlinearities within the input feature space due to the more flexible model structure, which results in better prediction capability; however, ANNs are more prone to overfitting the training data, and the training procedure takes much longer, especially when conducting a grid search over potential model architectures and hyperparameters. The ANN model forms are also typically much more complex; however, a single model can predict multiple outputs. Though AANNT streamlines the model training and evaluation, the models typically consist of various weights and bias terms, which the user would have to manually assemble using Eq. (3) for application outside of the AANNT framework.

## V. Conclusions

This work compared ANN and MOF prediction models that were trained over aerodynamic and aeroacoustic quantities generated using low-fidelity tools for isolated hovering sUAS rotors. It was shown that the ANN models developed using AANNT exhibited slightly less prediction error when compared to the MOF models; however, both ANN and MOF models accurately predicted all aerodynamic and aeroacoustic quantities except for  $\overline{SPL}_{th}$  and  $\overline{SPL}_{lo}$  at observers located directly above and below the rotor where an acoustic null region was present. Quantitative and qualitative prediction model performance were also illustrated for both prediction model types. A characterization study was performed using Sobol' sensitivity indices calculated by AANNT, which showed that both the ANN and MOF models exhibit similar sensitivity results, indicating that both model types produce analogous representations of the underlying physical relationship between the input features and output quantities. Characterization results showed that input features related to the spanwise sectional blade lift and spanwise sectional blade drag were highly significant to the aerodynamic thrust and power prediction models, respectively. It was also shown that the aeroacoustic prediction models were dominated by variations in  $\Omega$  and  $R$ , which affect the Doppler factor for tonal noise and the spanwise  $Re$  for broadband noise.

A potential application for the prediction models developed in this work is aerodynamic and aeroacoustic rotor design optimization, since hover is the most aerodynamically demanding and noisiest operating condition. Though this work only included isolated hovering rotor conditions, the established prediction modeling frameworks could be used for vehicle specific characterization studies or extended to include other, less noisy flight conditions for full flight-envelope investigation and ultimately, aerodynamic and aeroacoustic flight-trajectory optimization.

## VI. Acknowledgments

This work was funded by the NASA Revolutionary Vertical Lift Technology (RVLT) and the Transformational Tools and Technologies (TTT) projects.

## References

- [1] Thurman, C. S., Zawodny, N. S., Pettingill, N. A., Lopes, L. V., and Baeder, J. D., "Physics-informed Broadband Noise Source Identification and Prediction of an Ideally Twisted Rotor," *AIAA SciTech 2021 Forum*, AIAA Paper 2021-1925, Virtual, January 2021.
- [2] Thurman, C. S., Zawodny, N. S., and Baeder, J. D., "Computational Prediction of Broadband Noise from a Representative Small Unmanned Aerial System Rotor," *VFS International 76th Annual Forum & Technology Display*, Virtual, October 2020.
- [3] Zawodny, N. S., Boyd Jr., D. D., and Burley, C. L., "Acoustic Characterization and Prediction of Representative, Small-Scale Rotary-Wing Unmanned Aircraft System Components," *AHS International 72nd Annual Forum & Technology Display*, West Palm Beach, FL, May 2016.
- [4] Li, S., and Lee, S., "UCD-QuietFly: A New Program to Predict Multi-Rotor eVTOL Broadband Noise," *2020 VFS Aeromechanics for Advanced Vertical Flight Technical Meeting*, San Jose, CA, January 2020.

- [5] Ffowcs Williams, J. E., and Hawkings, D. L., “Sound Generation by Turbulence and Surfaces in Arbitrary Motion,” *Philosophical Transactions of the Royal Society of London. Series A, Mathematical and Physical Sciences*, Vol. 264, No. 1151, 1969, pp. 321–342.
- [6] Thurman, C. S., Zawodny, N. S., and Pettingill, N. A., “The Effect of Boundary Layer Character on Stochastic Rotor Blade Vortex Shedding Noise,” *VFS International 78th Annual Forum & Technology Display*, Fort Worth, TX, May 2022.
- [7] Thurman, C. S., “Computational Study of Boundary Layer Effects on Stochastic Rotor Blade Vortex Shedding Noise,” *Aerospace Science and Technology*, Vol. 131A, No. 107983, 2022.
- [8] Amiet, R., “Acoustic Radiation from an Airfoil in a Turbulent Stream,” *Journal of Sound and Vibration*, Vol. 41, No. 4, 1975, pp. 407–420.
- [9] Brooks, T. F., Pope, D. S., and Marcolini, M. A., “Airfoil Self-Noise and Prediction,” NASA RP 1218, 1989.
- [10] Burley, C. L., and Brooks, T. F., “Rotor Broadband Noise Prediction with Comparison to Model Data,” *Journal of the American Helicopter Society*, Vol. 49, No. 1, 2004, pp. 28–42.
- [11] Pettingill, N. A., and Zawodny, N. S., “Identification and Prediction of Broadband Noise for a Small Quadcopter,” *VFS International 75th Annual Forum & Technology Display*, Philadelphia, PA, May 2019.
- [12] Pettingill, N. A., Zawodny, N. S., Thurman, C. S., and Lopes, L. V., “Acoustic and Performance Characteristics of an Ideally Twisted Rotor in Hover,” *AIAA SciTech 2021 Forum*, AIAA Paper 2021–1928, Virtual, January 2021.
- [13] Thurman, C. S., and Zawodny, N. S., “Aeroacoustic Characterization of Optimum Hovering Rotors using Artificial Neural Network,” *VFS International 77th Annual Forum & Technology Display*, Virtual, May 2021.
- [14] Thurman, C. S., “Surrogate Modeling and Characterization of Blade-Wake Interaction Noise for Hovering sUAS Rotors using Artificial Neural Networks,” Ph.D. thesis, University of Maryland, College Park, MD, July 2022.
- [15] Li, S., and Lee, S., “A Machine Learning-Based Fast Prediction of Rotorcraft Broadband Noise,” *AIAA AVIATION 2020 Forum*, AIAA Paper 2020–2588, Virtual, June 2020.
- [16] Poggi, C., Rossetti, M., Serafini, J., Bernardini, G., Gennaretti, M., and Iemma, U., “Neural Network Meta-Modelling for an Efficient Prediction of Propeller Array Acoustic Signature,” *Aerospace Science and Technology*, Vol. 130, No. 107910, 2022.
- [17] Simmons, B. M., Buning, P. G., and Murphy, P. C., “Full-Envelope Aero-Propulsive Model Identification for Lift+Cruise Aircraft using Computational Experiments,” *AIAA AVIATION 2021 Forum*, AIAA Paper 2021–3170, Virtual, August 2021.
- [18] Simmons, B. M., “System Identification for Propellers at High Incidence Angles,” *Journal of Aircraft*, Vol. 58, No. 6, 2021, pp. 1336–1350.
- [19] Montgomery, D. C., *Design and analysis of experiments*, John Wiley & Sons, 2017.
- [20] Fang, K.-T., Li, R., and Sudjianto, A., *Design and modeling for computer experiments*, Chapman and Hall/CRC, 2005.
- [21] Fang, K.-T., Lin, D., Winker, P., and Zhang, Y., “Uniform Design: Theory and Application,” *Technometrics*, Vol. 42, No. 3, 2000, pp. 237–248.
- [22] Hickernell, F. J., “A Generalized Discrepancy and Quadrature Error Bound,” *Mathematics of Computation*, Vol. 67, No. 221, 1998, pp. 299–322.
- [23] Johnson, W., *CAMRAD II: Comprehensive Analytical Model of Rotorcraft Aerodynamics and Dynamics, Vols. I – VII*, Johnson Aeronautics, 2020.
- [24] Nichols, R. H., Tramel, R. W., and Buning, P. G., *Solver and Turbulence Model Upgrades to OVERFLOW 2 for Unsteady and High-Speed Applications*, AIAA Paper 2006–2824, San Francisco, CA, June 2006.
- [25] Tramel, R. W., Nichols, R. H., and Buning, P. G., “Addition of Improved Shock-Capturing Schemes to OVERFLOW 2.1,” *19th AIAA Computational Fluid Dynamics Conference*, AIAA Paper 2009–3988, San Antonio, TX, June 2009.
- [26] Medida, S., and Baeder, J. D., “Application of the Correlation-Based  $\gamma - \overline{Re}_{\theta_t}$  Transition Model to the Spalart-Allmaras Turbulence Model,” *20th AIAA Computational Fluid Dynamics Conference*, AIAA Paper 2011–3979, Honolulu, HI, June 2011.
- [27] Boyd, D. D., Lopes, L. V., and Bain, J., “UAM Noise Working Group (UNWG) Meeting Subgroup 1: Tools and Technologies,” *UAM Noise Working Group Meeting*, Hampton, VA, April 2022.

- [28] Farassat, F., and Succi, G. P., “The Prediction of Helicopter Discrete Frequency Noise,” *Vertica*, Vol. 7, No. 4, 1983, pp. 309–320.
- [29] Lopes, L. V., “Compact Assumption Applied to Monopole Term of Farassat’s Formulations,” *Journal of Aircraft*, Vol. 54, No. 5, 2017, pp. 1649–1663.
- [30] Rumelhart, D. E., Hinton, G. E., and Williams, R. J., “Learning Representations by Back-propagating Errors,” *Nature*, Vol. 323, 1986, pp. 533–536.
- [31] Thurman, C. S., “The ANOPP2 Artificial Neural Network Tool (AANNT) Reference Manual,” NASA TM 20220014856, 2022.
- [32] Hendrycks, D., and Gimpel, K., “Gaussian Error Linear Units (GELUs),” *arXiv*, Vol. 1606, No. 08415, 2016.
- [33] Ramachandran, P., Zoph, B., and Le, Q. V., “Searching for Activation Functions,” *arXiv*, Vol. 1710, No. 05941, 2017.
- [34] Huber, P. J., “Robust Estimation of a Location Parameter,” *The Annals of Mathematical Statistics*, Vol. 35, No. 1, 1964, pp. 73–101.
- [35] Kingma, D. P., and Lei Ba, J., “Adam: A Method for Stochastic Optimization,” *3rd International Conference on Learning Representations*, San Diego, CA, May 2015.
- [36] Morelli, E. A., “Global Nonlinear Aerodynamic Modeling Using Multivariate Orthogonal Functions,” *Journal of Aircraft*, Vol. 32, No. 2, 1995, pp. 270–277.
- [37] Morelli, E. A., and Klein, V., *Aircraft System Identification: Theory and Practice*, 2<sup>nd</sup> ed., Sunflyte Enterprises, Williamsburg, VA, 2016.
- [38] Barron, A. R., “Predicted Squared Error: A Criterion for Automatic Model Selection,” *Self-Organizing Methods in Modeling*, Farlow, S. J., Ed., Marcel Dekker, Inc., New York, NY, 1984, pp. 87–104.
- [39] Morelli, E. A., “Real-Time Global Nonlinear Aerodynamic Modeling for Learn-To-Fly,” *AIAA Atmospheric Flight Mechanics Conference*, AIAA Paper 2016–2010, San Diego, CA, 2016.
- [40] Morelli, E. A., “Practical Aspects of Real-Time Modeling for the Learn-To-Fly Concept,” *2018 Atmospheric Flight Mechanics Conference*, AIAA Paper 2018–3309, Atlanta, GA, 2018.
- [41] Morelli, E. A., and DeLoach, R., “Response Surface Modeling using Multivariate Orthogonal Functions,” *39th AIAA Aerospace Sciences Meeting and Exhibit*, AIAA Paper 2001–0168, Reno, NV, January 2001.
- [42] Morelli, E. A., and DeLoach, R., “Wind Tunnel Database Development Using Modern Experiment Design and Multivariate Orthogonal Functions,” *41st Aerospace Sciences Meeting and Exhibit*, AIAA Paper 2003–653, Reno, NV, January 2003.
- [43] Simmons, B. M., “Efficient Variable-Pitch Propeller Aerodynamic Model Development for Vectored-Thrust eVTOL Aircraft,” *AIAA AVIATION 2022 Forum*, AIAA Paper 2022–3817, Chicago, IL, 2022.
- [44] Morelli, E. A., *System IDentification Programs for AirCRAFT (SIDPAC) Version 4.1*, NASA Langley Research Center, <https://software.nasa.gov/software/LAR-16100-1>, Retrieved November 2022.
- [45] Saltelli, A., “Making Best use of Model Evaluations to Compute Sensitivity Indices,” *Computer Physics Communications*, Vol. 145, No. 2, 2002, pp. 280–297.